Advanced Materials

ADVANCED MATERIALS
www.advmat.de

RESEARCH ARTICLE

A Ferromagnetic Polar Metal With Efficient Electrical Switch of Magnetism

Wenxiao Shi[1,2] | Huan Lei[1] | De Hou[3] | Haojin Wang[4] | Zhou Wang[3] | Jiahui Cai[1] | Zhongqi Deng[1] | Yu Xie[5] | Junting Zhang[5] | Daming Tian[6] | Hui Zhang[6] | Zhe Yuan[7] | Bowen Yu[1,2] | Tianlin Zhou[1,2] | Jianjie Li[1,2] | Jing Zhang[8] | Jing Wu[9] | Zezhong Zhang[9] | Nicolas Gauquelin[10] | Banggui Liu[1,2] | Fengxia Hu[1,2] | Jirong Sun[1,2] | Johan Verbeeck[10] | Yuanchang Li[4] | Zhen Chen[1,2] | Zhigao Sheng[3] | Yuansha Chen[1,2] | Yunzhong Chen[1,2] | Baogen Shen[1,2,11,12]

[1]Beijing National Laboratory For Condensed Matter Physics and Institute of Physics, Chinese Academy of Sciences, Beijing, China | [2]School of Physical Sciences, University of Chinese Academy of Sciences, Beijing, China | [3]High Magnetic Field Laboratory, HFIPS, Chinese Academy of Sciences, Hefei, China | [4]Key Lab of Advanced Optoelectronic Quantum Architecture and Measurement, and School of Interdisciplinary Science, Beijing Institute of Technology, Beijing, China | [5]School of Materials Science and Physics, China University of Mining and Technology, Xuzhou, China | [6]School of Integrated Circuit Science and Engineering, Beihang University, Beijing, China | [7]Interdisciplinary Center for Theoretical Physics and Information Sciences, Fudan University, Shanghai, China | [8]Songshan Lake Materials Laboratory, Dongguan, Guangdong, China | [9]AI For Science Institute, Beijing, China | [10]Electron Microscopy for Materials Science (EMAT), University of Antwerp, Antwerp, Belgium | [11]Ganjiang Innovation Academy, Chinese Academy of Sciences, Ganzhou, Jiangxi, China | [12]CAS Key Laboratory of Magnetic Materials and Devices and Zhejiang Province Key Laboratory of Magnetic Materials and Application Technology, Ningbo Institute of Materials Technology and Engineering, Chinese Academy of Sciences, Ningbo, China

Correspondence: Yuanchang Li (yuancli@bit.edu.cn) | Zhen Chen (zhen.chen@iphy.ac.cn) | Zhigao Sheng (zhigaosheng@hmfl.ac.cn) | Yuansha Chen (yschen@iphy.ac.cn) | Yunzhong Chen (yzchen@iphy.ac.cn)

Received: 17 March 2026 | **Revised:** 16 June 2026 | **Accepted:** 9 July 2026

Keywords: condensed matter physics | current density | ferromagnetism | heterojunction | magnetism | magnetization | materials science | multiferroics | spintronics | superlattice

ABSTRACT

Materials that host intrinsic coexisting ferromagnetism, polar distortion, and metallicity, a ferromagnetic polar metal (FPM), can combine the advantages of both multiferroics and polar metals, and thus are expected to provide unforeseen opportunities for spintronics with ultra-low-power consumption. However, generalizable routes for creating FPMs with strong coupling between itinerant ferromagnetism and polar distortions are still limited. Meanwhile, efficient electrical control of magnetism in such systems remains unexplored. Herein, we introduce a design strategy based on interfacial oxygen-octahedral-rotation mismatch to create an intrinsic FPM state in superlattices composed of two nonpolar perovskites, $SrRuO_3$ and $CaTiO_3$. Unlike previous layered oxide systems, which often result in in-plane polarization, our superlattice FPM exhibits pronounced out-of-plane polar displacements directly within the perpendicular ferromagnetic RuO_6 metal network, enabling a strong entanglement between magnetic order and polarity. Consequently, the Rashba spin-orbit torque in the superlattice FPM gives rise to extraordinary current-driven magnetization self-switching at a current density as low as 2.5×10^5 A cm^{-2}, about two orders of magnitude lower than that of conventional heavy-metal/ferromagnet heterostructures. Our work not only identifies a robust strategy for accessing FPM states but also provides a promising platform for exploring ultra-low-power spintronic devices.

Wenxiao Shi, Huan Lei, De Hou, and Haojin Wang contributed equally to this work.

1 | Introduction

Polarity and metallicity have traditionally been viewed as mutually exclusive, because free carriers in a metal are expected to efficiently screen internal electric fields and thereby suppress the ferroelectric-like atomic displacements that define a polar state [1, 2]. This canonical view was first challenged in 1965 by Anderson and Blount, who proposed that a "ferroelectric metal" could be realized in the limit of weak electron-lattice coupling [3]. Experimental verification has been highly challenging, and it was not until decades later that the first polar metal, the perovskite $LiOsO_3$, was discovered [4]. The coexistence of polarization and metallicity in this ABO_3 perovskite oxide was rationalized by weak coupling between the A- and B-site cation sublattices: A-site cations can undergo polar displacements while the B-site sublattice simultaneously maintains metallic conduction. This guiding principle subsequently led to the discovery of other polar metallic systems, including strained $NdNiO_3$ [5] and electron-doped $BaTiO_3$ [6].

While this breakthrough accelerated the search for polar metals, incorporating spin order as a third degree of freedom to create magnetic polar metals, remains a formidable challenge. This difficulty stems from the so-called d^0 rule in simple ABO_3 perovskites: conventional ferroelectricity typically originates from the second-order Jahn–Teller effect, which favors empty d orbitals, whereas magnetism requires partially filled d orbitals [7, 8]. To circumvent this incompatibility, hybrid improper ferroelectricity (HIF) has been proposed as a geometric route to induce polarity via trilinear coupling between the nonpolar octahedral rotation and the polar mode [9, 10]. Since its proposal, HIF has been explored primarily in layered oxides [11–13] and perovskite superlattices [10, 14], which likely underlie the recent creation of polar metallic oxides such as the polar antiferromagnets $Ca_3Ru_2O_7$ [15, 16] and $Sr_3Co_2O_7$ [17], as well as the polar ferromagnet $Ca_3Co_3O_8$ [18]. However, layered systems are subject to intrinsic structural constraints. Rock-salt AO layers interrupt structural continuity [11, 12], defining a 2D layered architecture, which results in a massive depolarization field that restricts the polarization to be in-plane. In practice, out-of-plane polarization is often preferred for functional devices [12, 19]. Magnetically, exchange interactions in these layered systems are typically dominated by antiferromagnetic coupling (e.g., $Ca_3Ru_2O_7$ [15, 16] and $Sr_3Co_2O_7$ [17]) or by in-plane magnetic anisotropy (e.g., $Ca_3Co_3O_8$ [18]), preventing strong ferromagnetism with perpendicular magnetic anisotropy (PMA) [20]. More importantly, owing to their limited magnetoelectric coupling, efficient electrical control of magnetism has not yet been achieved in these layered oxides—the very capability that multiferroics most eagerly pursue. In principle, atomically engineered ABO_3 perovskite superlattices (SLs) can overcome these disadvantages by maintaining a continuous octahedral network [10]. Therefore, the key challenge is to create a magnetic polar metal in which out-of-plane polarity, itinerant ferromagnetism, and PMA coexist within a continuous BO_6 network.

Recent advances in self-spin-orbit torque (self-SOT) switching have demonstrated electrical control of magnetic order in low-symmetry magnetic systems, including the van der Waals ferromagnet Fe_3GeTe_2 [21–24], non-collinear antiferromagnet $Ni_{1/3}NbS_2$ [25], and topological antiferromagnet $Co_{1/3}TaS_2$ [26]. These studies establish symmetry-enabled self-SOT as an efficient route for the electrical control of magnetism. Ferromagnetic polar metals (FPMs) provide a particularly attractive platform for self-SOT switching, because their polar distortions can generate a Rashba-type spin accumulation under an applied charge current. This spin accumulation exerts an anti-damping torque directly on the magnetization, thereby enabling magnetization self-switching. We therefore studied a distinct design strategy based on interfacial oxygen-octahedral-rotation (OOR) mismatch to realize an intrinsic FPM state in SLs composed of two non-polar perovskites. We deliberately choose the itinerant ferromagnet $SrRuO_3$ (SRO), characterized by strong spin-orbit coupling (SOC) and robust PMA [27, 28], and the wide-bandgap insulator $CaTiO_3$ (CTO) as building blocks. Although both materials crystallize in a $GdFeO_3$-type orthorhombic structure in bulk, their OOR patterns become incompatible when grown as thin films. SRO films typically exhibit the $a^-a^-c^+$ rotation pattern [27], whereas CTO films favor the $a^-b^+a^-$ pattern [29, 30]. As schematically shown in Figure 1a, the conflict between in-phase (b^+) rotations in CTO and out-of-phase (a^-) rotations in SRO along the pseudo-cubic b-axis triggers a cooperative structural distortion, forcing the RuO_6 and TiO_6 octahedra into a polar configuration (Figure 1b).

Herein, we report pronounced out-of-plane polar displacements of the magnetic B-site Ru cations in SRO/CTO SLs, which are fundamentally different from the conventional A-site driven HIF mechanism that is typically restricted to in-plane polarization. These atomic-scale displacements are directly visualized by multi-slice electron ptychography (MEP). The resulting polarization is further corroborated by robust optical second harmonic generation (SHG) signals that persist up to room temperature. More importantly, simultaneous space-inversion symmetry breaking (polarity) and time-reversal symmetry breaking (ferromagnetism) within the same RuO_6 sublattice unlock strong magnetoelectric coupling and emergent phenomena. Specifically, the space-symmetry breaking generates strong Rashba-SOC [31–36], enabling efficient current-driven magnetization self-switching at an ultra-low critical current density of 2.5×10^5 A cm^{-2}. This value is one or two orders of magnitude smaller than those of other complex oxides [37–40] and conventional heavy-metal/ferromagnet systems [41–43]. Leveraging the multi-interface advantages of the SL architecture, we achieve a switching ratio of 75 %, the highest reported among self-switching systems to date. The low switching energy, combined with the scalability of oxide epitaxy, positions FPMs as promising building blocks for next-generation spintronic logic, nonvolatile memory, and neuromorphic computing architectures.

2 | Results

2.1 | SRO/CTO Superlattices With Strong Oxygen Octahedral Rotation Mismatch

The high-quality $(SRO_n/CTO_3)_{10}$ SLs with alternately stacked SRO and CTO layers were epitaxially grown on (001)-oriented $SrTiO_3$ (STO) substrates by pulsed laser deposition. Each period of the SL is composed of n unit cells of SRO and 3-unit cells of CTO, where n ranges from 4, 6 to 8. The out-of-plane lattice structure

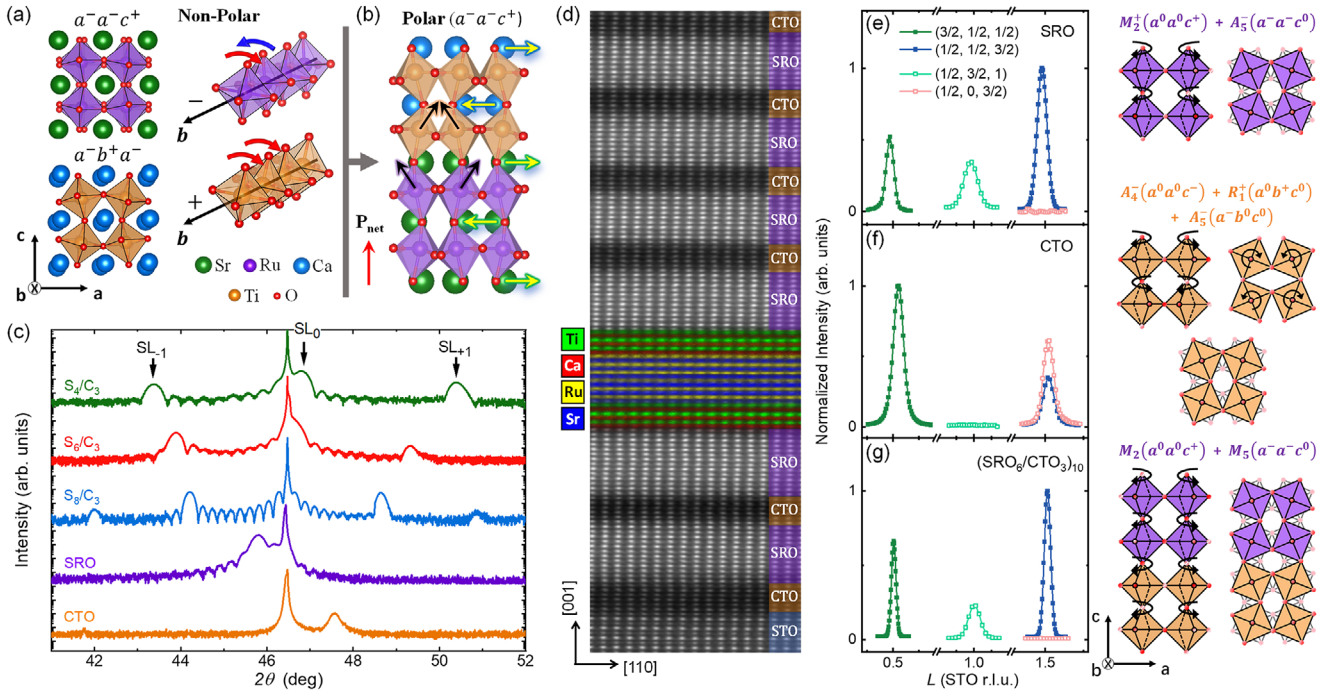

FIGURE 1 | (a) Schematic views of lattice structures of SRO with an $a^-a^-c^+$ OOR pattern (up panel) and CTO with an $a^-b^+a^-$ OOR pattern (bottom panel). Purple and orange octahedra represent RuO_6 and TiO_6, respectively. The right panel shows the out-of-phase rotation (a^-) and in-phase rotation (b^+) along the *b*-axis for the SRO and CTO, respectively. (b) Schematic illustration of the polar structure. (c) Out-of-plane θ–2θ scans for the SRO/CTO SLs on (001)-oriented STO substrate. SL_0 indicates the (002) main peak and $SL_{\pm1}$ indicate the satellite peaks. (d) Enlarged cross-sectional HAADF-STEM image of the SL, together with the corresponding EDS elemental maps of Ti, Ca, Ru, and Sr, showing periodic SRO/CTO stacking and chemically sharp interfaces. (e) Half-order peaks obtained from the SRO, (f) CTO, and (g) SRO/CTO SL on STO substrates. On the right is a schematic of the irreducible representations for the corresponding OOR modes.

of the SLs was analyzed by X-ray diffraction (XRD), as shown in Figure 1c. For comparison, data from bare SRO (c_{SRO} = 3.95 Å) and CTO (c_{CTO} = 3.80 Å) films are also presented, respectively. Clear (002) Bragg peaks with thickness fringes indicate high crystallinity and a flat surface of the samples. Moreover, distinct satellite peaks are detected, shifting toward the (002) main peak as *n* increases, which is a general feature of the XRD spectra for SL structures. Based on the results of θ–2θ scanning, the average *c*-axis lattice constants of the SLs increase smoothly from 3.88 to 3.91 Å as the SRO thickness (*n*) increases from 4 to 8 u.c. (Figure S1a). To determine the in-plane strain state of the SLs, reciprocal space mapping (RSM) around the (103) reflection was performed. Taking $(SRO_6/CTO_3)_{10}$ SL as an example, the SL diffraction spots (marked by a red arrow in Figure S1b) are vertically aligned with those of the substrate, that is, the SL is coherently strained to the substrate without lattice relaxation, giving rise to $a = b = 3.905$ Å. The high-quality epitaxial growth of the SL was further confirmed by cross-sectional scanning transmission electron microscope (STEM) image (Figure 1d), where the energy-dispersive X-ray spectroscopy (EDS) mappings reveal distinct Ti (green), Ru (yellow), Ca (red) and Sr (blue) atomic positions with no interdiffusion, thereby confirming perfectly coherent stacking of the SRO and CTO layers, further confirmed by EELS like scan analysis (Figure S2).

The OOR patterns of the SRO, CTO, and the SL were identified unambiguously by mapping the half-integer Bragg peaks via synchrotron XRD [44, 45]. Generally, the half-integer Bragg peaks arise when the pseudo-cubic unit cell is doubled by octahedral rotations, and their presence or absence can provide a direct fingerprint of the underlying crystal symmetry and tilt system [46, 47]. In the reference SRO film, we confirmed an $a^-a^-c^+$ tilt pattern (Figure 1e): the half-integer peaks such as (1/2, 1/2, 3/2) signal the out-of-phase rotations along the in-plane axes, while the concurrent (1/2, 3/2, 1) reflection whose out-of-plane index is an integer confirms an in-phase rotation along *c*, i.e. the $a^-a^-c^+$ assignment (corresponding to the combined irreducible representations $M_2^+ \oplus A_5^-$). Conversely, the reference CTO film exhibited an $a^-b^+a^-$ tilt pattern (corresponding to the combined irreducible representations $A_4^- \oplus R_1^+ \oplus A_5^-$): evidenced by the (1/2, 0, 3/2) reflections that signify in-phase rotation along its in-plane axis (Figure 1f). In contrast, a dramatic structural transition is observed in the diffraction pattern of the $(SRO_6/CTO_3)_{10}$ SL (Figure 1g). Reflections characteristic of the CTO $a^-b^+a^-$ pattern, specifically (1/2, 0, 3/2), completely disappear. In their place, reflections corresponding to the $a^-a^-c^+$ pattern, the (1/2, 3/2, 1) peak, emerge. This result provides definitive evidence that the octahedral rotation in the CTO layers transitions from its native $a^-b^+a^-$pattern to the $a^-a^-c^+$ pattern, which is then coherently imposed throughout the entire heterostructure (corresponding to the combined irreducible representations $M_2 \oplus M_5$). To understand the energetic origin and symmetry consequences of this structural reconstruction, we performed density functional theory (DFT) calculations exploring all 10 possible rotational types (Figure S3). The calculations confirm that the experimentally observed $a^-a^-c^+$ pattern corresponds to the ground state with the lowest total energy. Crucially, symmetry analysis reveals that this specific rotational configuration reduces the crystallographic

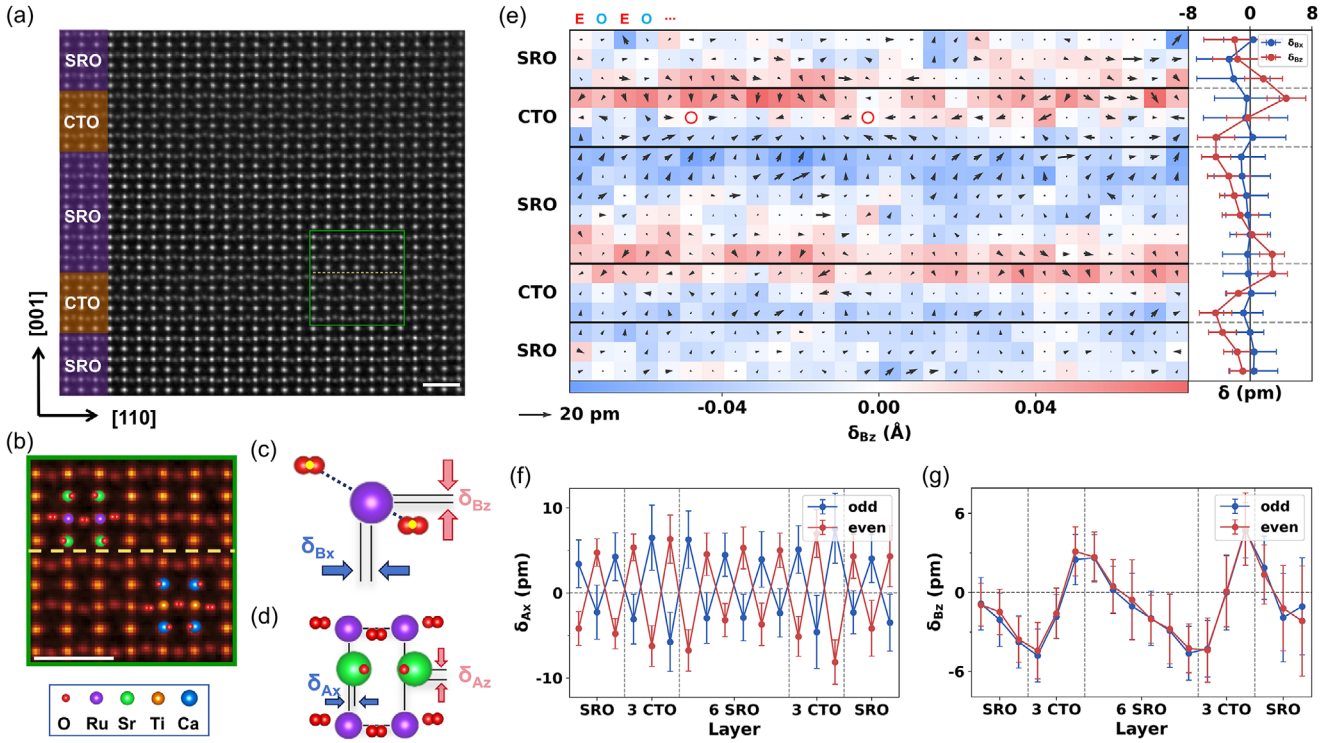

FIGURE 2 | (a) Atomic-resolution MEP reconstruction of the $(SRO_6/CTO_3)_{10}$ SL acquired along the [110] zone axis. Alternating SRO (purple) and CTO (orange) blocks stack along [001]; arrows indicate crystallographic directions. The green box marks the region enlarged in (b). (b) Locally magnified MEP views from (a). Top: SRO region; bottom: CTO region, separated by a dashed line. Overlaid colored circles mark the atomic columns (legend: O, Ru, Sr, Ti, and Ca). (c) Schematic definition of the local B-site polarization displacement in an ABO_3 lattice. The in-plane (δ_{Bx}) and out-of-plane (δ_{Bz}) components are measured from the B-site cation (Ru/Ti) to the center of its adjacent in-plane oxygen pair (red spheres). (d) Schematic definition of the A-site (Sr/Ca) polarization. Here, δ_{Ax} and δ_{Az} are defined as the displacement of the A-site relative to the midpoint between the neighboring upper and lower B-site planes. (e) Two-dimensional map of B-site polarization vectors. Background colors represent δ_{Bz} (red, positive; blue, negative), while black arrows show the in-plane component. The even (E) and odd (O) atomic columns along [110] are labeled at the top. Right: layer-resolved averages of the B-site displacement magnitude along x (δ_{Bx}, blue) and z (δ_{Bz}, red). Scale bar in the lower-left corner: 20 pm. Red circles indicate manually removed outliers. (f) Layer-resolved A-site δ_{Ax} for odd (blue) and even (red) columns. Error bars represent one standard deviation. (g) Layer-resolved B-site δ_{Bz} for odd (blue) and even (red) columns. Error bars represent one standard deviation. The white line in the image represents 1 nm.

symmetry to the polar space group *Pc*, corresponding to the polar point group C_s. Within this noncentrosymmetric framework, the geometric constraints necessitate cooperative polar displacements of both the Ru^{4+} and Ti^{4+} cations away from their centrosymmetric positions, as also visualized by the MEP results presented next, thereby establishing a robust, macroscopic polar state throughout the SL.

2.2 | Microscopic Signature of the Polarity

Aberration-corrected STEM and MEP were performed to directly probe the atomic-scale origin of the possible polarity [48]. Figure 2a presents an atomic-resolution MEP reconstruction showing the sharp SRO and CTO layers in the $(SRO_6/CTO_3)_{10}$ SL. Octahedral rotations can be directly visualized in the enlarged atomic images in Figure 2b. The polarization is considered from both the B-site cation displacement corresponding to the center of the oxygen sub-lattice (δ_{Bx} and δ_{Bz}) and A-site displacement corresponding to the B sublattice (δ_{Ax} and δ_{Az}), as illustrated in Figure 2c,d. Figure 2e maps the unit-cell-resolved two-dimensional displacements of the B-site cations, with the line plot on the right showing the layer-averaged magnitude. The B-site displacements reach up to ±5 pm, while the variation within each layer is about 1.3 pm, close to the measurement precision of MEP with additional small lattice fluctuations. Layer-resolved analysis shows that the B-site cations exhibit essentially no net polarization along x: the positive and negative δ_{Bx} components cancel within each layer. In contrast, the out-of-plane component δ_{Bz} is finite and exhibits a clear sign reversal between neighboring SRO and CTO blocks, as highlighted by the alternating red and blue bands in the polarization heat map in Figure 2e. Within both the SRO and CTO slabs, δ_{Bz} reverses sign between the top and bottom interfaces, giving a sawtooth-like profile in which the magnitude peaks (~ 5 pm) at the interfaces and decreases toward the layer interior. This indicates that the local polar distortion is strongly interface-centered and induced by the interfacial structural or electronic reconstruction.

The layer- and column-resolved line profiles in Figure 2f,g further clarify the symmetry of these displacements. For the A sublattice, the in-plane component δ_{Ax} shows a strict odd-even alternation along [110]: the even (E) and odd (O) columns possess equal but opposite x displacements in each layer, as seen in Figure 2f, yielding an antiferroelectric-like arrangement with vanishing net A-site polarization. By contrast, the out-of-plane B-site

displacement δ_{Bz} is almost identical for the odd and even columns (Figure 2g), demonstrating that the polar distortion along z is uniform within each layer and is dominated by the B-site cations. The combination of odd-even antiphase A-site shifts in x together with in-phase B-site shifts in z corresponds to a C_s point-group symmetry, fully consistent with the macroscopic SHG response. Overall, the atomic-displacement-vector maps reveal that the primary polar degree of freedom in the $(SRO_6/CTO_3)_{10}$ SL resides on the B-site cations, which develop sizable out-of-plane, interface-centered dipoles with negligible in-plane component, while the A-site cations form an antiferroelectric-like pattern that cancels macroscopically.

There is also a checkerboard-like modulation of the octahedral tilt determined from angles θ ($O\text{-}B_1\text{-}B_2$ shown in Figure S4c), with the average value of absolute $|\theta|$ of 5.9° and a standard deviation of 2.0°. The layer-averaged amplitude of octahedral rotation β ($B_1\text{-}O\text{-}B_2$ shown in Figure S4c) reaches a minimum of ~164° at the SRO/CTO interface and a maximum of ~171° at about the middle layer of SRO (Figure S4b), exhibiting a layer-by-layer wavelike variation and exceeding the values in single-layer SRO (163°) [49] and CTO (156°) [50]. It is noted that large OORs coexist with antipolar cation displacements, both of which are typically thought to suppress the ferroelectric mode [51]. Nevertheless, a mismatch of octahedral rotation patterns at the interface induces an out-of-plane polarization in SRO. This leads to the unusual co-stabilization of modes that are conventionally incompatible: OORs with ferroelectricity, and antipolar cation displacements with ferroelectricity. The net polarization arises from an unconventional microscopic distortion dominated by displacements of B-site cations relative to the geometric centers of the oxygen-octahedral sublattice.

2.3 | Macroscopic Evidence of Out-of-Plane Polarization

Macroscopic evidence of the FPM state in the SRO/CTO SL is also observed. Temperature-dependent magnetization measurements (Figure 3a) reveal a ferromagnetic ground state with a Curie temperature (T_c) of ~150 K, dominated primarily by the SRO sublayer [27]. Meanwhile, the system exhibits metallic behavior across the whole temperature range, as confirmed by the temperature-dependent resistivity curve in Figure 3b, which shows a clear kink at ~150 K where the ferromagnetic transition suppresses the spin-dependent scattering. Below T_c the data follow excellent T^2 dependence, characteristic of a Fermi-liquid-like behavior [52], whereas above T_c a linear T dependence is observed. The slight upturn at ~ 30 K is probably attributed to disorder-induced localization. The saturation magnetization is 1.2 μ_B/Ru, consistent with the typical value of SRO single layers (Figure S5). Notably, magnetic measurements reveal that the magnetic anisotropy is highly sensitive to the SRO layer thickness. Unlike the PMA observed in the $n = 6$, 8 SLs, the thinner $(SRO_4/CTO_3)_{10}$ SL exhibits in-plane magnetic anisotropy (Figure S6).

The macroscopic polarization was determined by optical second-harmonic generation (SHG) measurement with the experimental setup as shown in the inset of Figure 3d. For comparison, in addition to the SRO/CTO SL, we systematically characterized three reference samples (bare SRO, CTO, and STO substrate) under identical conditions using two complementary SHG geometries: normal incidence (0°), predominantly sensitive to in-plane polarization, and oblique incidence (45°), sensitive to both in-plane and out-of-plane components. Under normal incidence, the SL and all reference samples exhibited weak fourfold patterns with comparable amplitudes (maximum intensity ~ 28 a.u.) in both colinear polarization (XX) and cross-linear polarization (XY) geometries (Figure S7), indicating negligible in-plane polarization. In contrast, oblique-incidence measurements, obtained by rotating the linear polarization of either the incident or the detected beam, reveal a pronounced SHG signal from the SL with distinct polarization-angle dependences. Figure 3c presents the SHG polar plot for the SRO/CTO SL, measured with $P(S)$-polarized incident beams ($P(S)_{in}$) and $P(S)$-polarized output beams ($P(S)_{out}$). SHG signals for P_{in}, S_{in}, and P_{out} configurations exhibit twofold rotational symmetry, whereas the S_{out} signal shows fourfold rotational symmetry. To quantitatively determine the crystal point group of the SL, we fitted the angle-dependent SHG intensities using the appropriate second-order nonlinear susceptibility tensors [29, 53]. Experimental data for all configurations are in excellent agreement with the fitting curves dictated by the polar C_s point group (solid lines in Figure 3c). Moreover, the peak SHG intensity from the SRO/CTO SL under oblique incidence reaches 4358 a.u. (Figure 3d), two orders of magnitude stronger than that of the reference samples (SRO, CTO, and STO substrate, Figure S8), which is also much larger than that of the recently discovered $Ca_3Co_3O_8$ [18]. To further examine whether the polar response could arise solely from the built-in electric field associated with chemically inequivalent interfaces, we synthesized an interface-symmetrized $(SRO_6/STO_1/CTO_3)_{10}$ SL, in which one-unit-cell STO is inserted between SRO and CTO to make the two effective interfaces equivalent. This control sample still exhibits a pronounced SHG response with the same characteristic polar symmetry (Figure S9), demonstrating that strong out-of-plane polarity persists in the interface-symmetrized structure. Therefore, the observed polarity cannot be attributed only to the electrostatic asymmetry of inequivalent interfaces. Taken together with the negligible normal-incidence response, these results confirm that the strong polar signal arises primarily from an out-of-plane polar displacement, establishing the intrinsic polar structure of the SL. Notably, the SHG intensity is robust at 300 K, unambiguously confirming the realization of a room-temperature polar metal state. Moreover, as also shown in Figure 3a, the SHG intensity for P_{in} configurations shows a distinct anomaly near T_c (~ 150 K), indicating a strong interaction between polarity and ferromagnetism in the SRO sublayer (results for other configurations in Figure S10).

2.4 | Current-Driven Magnetization Self-Switching in SRO/CTO Superlattices Under Ultra-Low Current Density

The coexistence of polarity, metallicity, and ferromagnetism gives rise to a wealth of emergent phenomena. In particularly, the perpendicular electric field generated by interface polarization could break the symmetry of SRO and induce Rashba-splitting [31–36], as verified by first-principles calculations. To estimate the strength of Rashba-splitting, we employ an SL structure composed of six SRO and two CTO unit cells. Despite differing from the experimental three-CTO unit cell, we expect this model

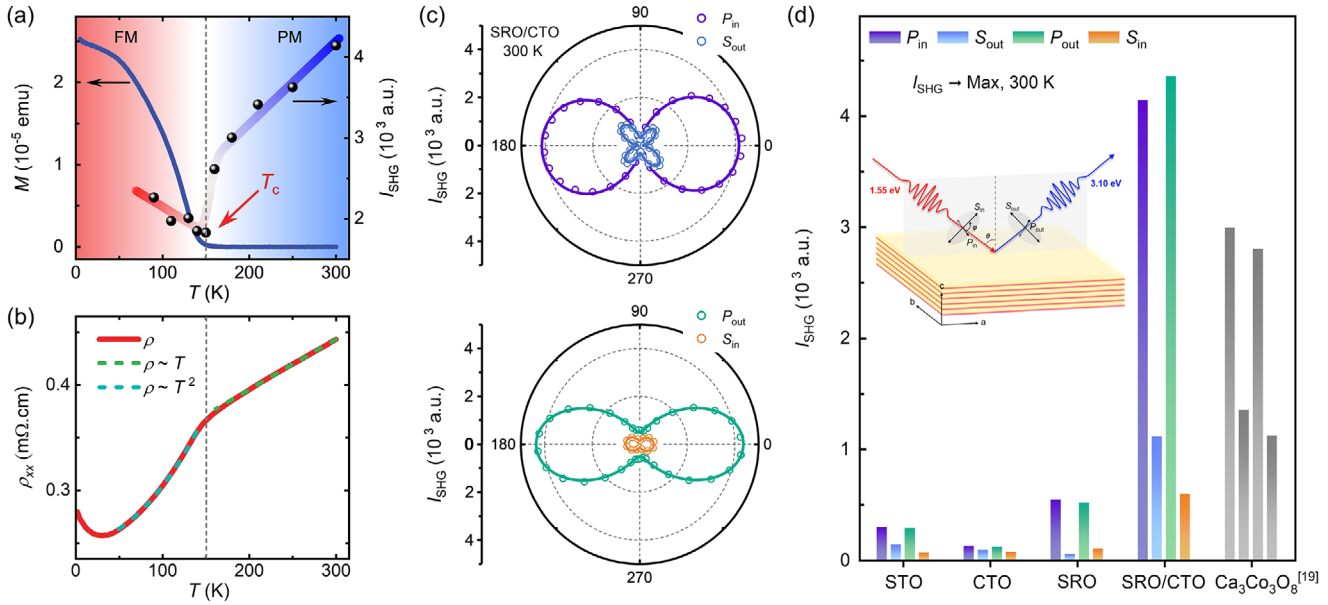

FIGURE 3 | (a) Temperature dependence of the magnetization (blue curve) and the SHG intensity in the P_{in} configuration (black dots) for the SRO/CTO SL. The magnetization was measured under an out-of-plane magnetic field of 500 Oe. (b) Resistivity versus the temperature curve of the SRO/CTO SL. (c) Polar plots of SHG intensity versus polarization angle for the SRO/CTO SL at 300 K with oblique incidence. $P(S)_{in}$: the input beam is fixed to the $P(S)$ polarization while revolving the polarization direction of the output beam; $P(S)_{out}$: the output beam is fixed to the $P(S)$ polarization while rotating the polarization direction of the input beam. Scattered circles are experimental data, and the solid lines are the fitting curves of experimental data with the C_s point group. (d) Maximum SHG intensities at room temperature for the SRO/CTO SL under various polarization configurations (P_{in}, S_{out}, P_{out}, and S_{in}), compared with reference samples (STO, CTO, SRO, and $Ca_3Co_3O_8$ [18]).

to capture the essential physics (Figure S11). The fully optimized SL structure exhibits the polar C_s point group, which aligns with experimental findings. This validates our design concept of achieving spontaneous polarization in two nonpolar materials through interface engineering. Charge analysis indicates that the formation of the interface indeed leads to electron accumulation on the SRO side and electron depletion on the CTO side, which provides direct evidence for the existence of a perpendicular electric field. Using the spin-projected band structure in Figure 4a, we estimate that the polar inversion-symmetry breaking generates a Rashba coefficient with a value of $\alpha_R = 0.125$ eV Å, which is highly significant for oxides [54, 55]. Due to the presence of a large Rashba effect in our SL, when an electric field is applied along the *x*/*y* direction, the inner and outer Fermi circles shift in opposite directions because their Fermi velocities are opposite. When current is applied along the *x* direction, the shift produces a nonequilibrium spin accumulation (σ_y), which generates an anti-damping torque in the form $\widehat{\tau_{ST}} = \hat{\boldsymbol{m}} \times \widehat{\sigma_y} \times \hat{\boldsymbol{m}}$ on the magnetization of the SL, enabling current-induced magnetization self-switching [35, 56–58]. A larger α_R corresponds to a stronger spin-orbit torque, implying that current-driven magnetization self-switching would be observed at lower thresholds. This microscopic picture is further supported by the polar monoclinic C_s symmetry of the SRO/CTO SLs, consistently established by SHG, MEP, and the DFT-relaxed structure. For the C_s point group, a magnetization-independent linear spin-charge response, $\sigma_i = \chi_{ij} J_j$, is symmetry-allowed [33], providing an independent symmetry basis for the current-induced spin accumulation.

To examine it, spin-orbit torque (SOT) switching measurements were performed on a 10 μm-wide Hall bar, as schematically shown in Figure 4(b), following the experimental procedure detailed in the Methods section. We measured the Hall resistivity ρ_H as a function of pulse current J_{pulse} in the FPM SRO/CTO SL. $\Delta\rho_H$ is defined as ρ_H relative to the center of the hysteresis loop. Spin accumulation generated by the injecting pulse currents reverses the magnetization of the SL, causing $\Delta\rho_H$ to flip. To confirm that this mechanism is unique to the polar SL interface, we first performed this measurement on a control sample of a single-layer SRO film using the same device geometry. Lacking the requisite interfacial symmetry breaking, this control film exhibited no current-induced switching, that is, no change in $\Delta\rho_H$ (Figure S12). In stark contrast, the SRO/CTO SL exhibits highly efficient switching, as shown in Figure 4(c). The hysteresis loop amplitude exhibits a non-monotonic dependence on auxiliary magnetic field (H_x), peaking at $H_x = 2000$ Oe before decreasing at higher fields. This behavior arises from the magnetization tilting along H_x and is typical of SOT switching [58]. The hysteresis direction reverses when H_x is reversed, confirming that magnetization is switched by current-driven SOT. Magnetization switching occurs at a critical current density (J_C) of 4.5×10^5 A cm^{-2}. No change in $\Delta\rho_H$ is observed at zero magnetic field. Within this measurement range, the maximum $\Delta\rho_H$ is ~ 0.32 μΩ cm, which is approximately 75% of full magnetization reversal. The Hall resistivity for the full magnetization switching under a magnetic field is shown in Figure S13. Notably, this is the highest switching ratio yet reported for a self-switching device [35, 39, 40, 57]. From these data, the threshold J_C was extracted (Figure 4e): J_C decreases with increasing H_x for $H_x < 2000$ Oe but increases for $H_x > 2000$ Oe. This is because, for $H_x < 2000$ Oe, the auxiliary magnetic fields assist SOT switching and reduce the switching current density, consistent with typical SOT behavior. However, for $H_x > 2000$ Oe, this field tilts part of the magnetization toward its own direction, driving switching closer to the film

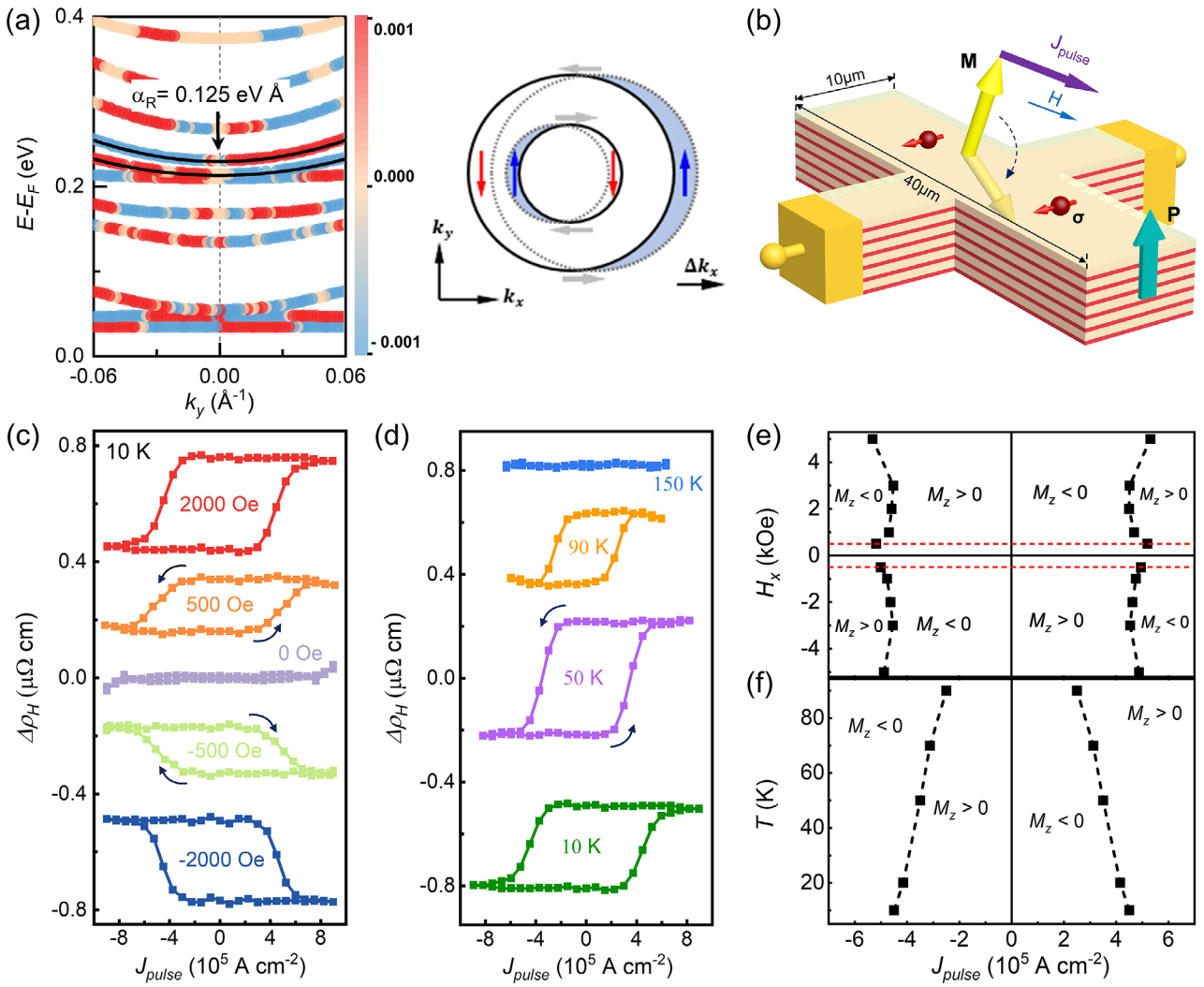

FIGURE 4 | (a) Left: Band structure for the SL structure around the Γ point along the K-Γ-K direction, with the color map indicating the spin-projected *x*-component. The two black lines near E-E_F = 0.22 eV are used to fit the Rashba coefficient α_R = 0.125 eV Å. See Supplementary Information for more details. Right: Principle of Rashba-Edelstein effect: The application of an electric field along the *x* direction causes the shift in Fermi surfaces (represented as Δk_x), resulting in spin accumulation. The black solid and dotted lines represent the Fermi surfaces without and with the application of an electric field, respectively. (b) Schematic illustration of magnetization switching in SRO/CTO SL caused by current-induced spin-orbit torque. The schematic defines the device geometry under polar C_s symmetry, including the writing-current direction J_{pulse}, the dominant out-of-plane polar axis $\boldsymbol{P}$, the induced spin accumulation $\boldsymbol{\sigma}$, the in-plane assisting field H_x and the perpendicular magnetization $\boldsymbol{M}$. (c) $\Delta\rho_H$-J_{pulse} loops under various H_x values at 10 K. (**d**) $\Delta\rho_H$-J_{pulse} loops at various T under H_x = +2000 Oe. The arrows express the sweep directions. The $\Delta\rho_H$ obtained by subtracting the average value of the ρ_H of each loop from the ρ_H is plotted. (**e**) Switching phase diagram of the SL about applied external magnetic field (H_x) and (**f**) temperature (T).

plane [32]. In this regime, large H_x hinders rather than aids the switching process, leading to an increase in switching current density. The impact of SRO layer thickness on SOT switching efficiency further corroborates the critical role of polarity. For the thicker $(SRO_8/CTO_3)_{10}$ sample, although it retains PMA, its switching performance is notably degraded. Since the polarity is primarily interface-induced and decays toward the SRO interior, increasing the SRO thickness leads to a reduction in the average B-site polar displacement (Figure S14). This directly weakens the Rashba-SOC strength, resulting in a significantly increased J_C and a decreased switching ratio for the 8-uc sample (Figure S15). This thickness dependence—where the 4-uc sample fails due to in-plane anisotropy and the 8-uc sample suffers from diluted polarity—identifies the 6-uc thickness as the optimal balance, strongly supporting our conclusion that the ultra-low current switching originates from the polarity-induced giant Rashba effect. To further examine the impact of CTO layer thickness on SOT switching efficiency, we measured the current-induced switching behavior of the $(SRO_6/CTO_2)_{10}$ sample. Although the 2-uc CTO sample exhibits a slightly lower critical switching current density, its switching ratio is only approximately 40%, substantially smaller than that of the 3-uc CTO sample (75%) (Figure S15).

In addition, the temperature dependence of SOT switching in the SL is shown in Figure 4d. The same counter-clockwise $\Delta\rho_H$-J_{pulse} loop remains stable up to 90 K. The SOT magnetization switching loop disappears above T_C ~150 K. As shown in Figure 4f, J_C

decreases with increasing temperature, owing to the reduced saturation magnetization and weakened magnetic anisotropy (Figure S16). Using the longitudinal resistivity ρ_{xx} as an internal thermometer [26], the Joule-heating-induced temperature rises at the critical switching current density are estimated to be only 9.8, 3.4, and 1.6 K at base temperatures of 10, 50, and 90 K, respectively, confirming that the device remains below T_c ~150 K during switching (Figure S17). Thermal fluctuations may also assist the magnetization in overcoming the switching energy barrier, further reducing J_C. The lowest critical switching current density obtained is $\sim 2.5 \times 10^5$ A cm^{-2} at $T = 90$ K. This value is approximately two orders of magnitude lower than the typical values of $\sim 10^7$ A cm^{-2} required for conventional heavy-metal/ferromagnet bilayers such as Pt/Co and Ta/CoFeB [41–43]. Furthermore, it is also approximately one order of magnitude lower than the $\sim 10^6$ A cm^{-2} reported for state-of-the-art all-oxide heterostructures such as $SrIrO_3/SrRuO_3$ or single-layer $SrRuO_3$ systems [37–40]. This superior performance stems from two key factors: first, operating within a single material eliminates interfacial spin-memory loss and scattering that typically limit the efficiency of bilayer heterostructure systems. Second, and more fundamentally, the polar system hosts a large intrinsic Rashba effect that enables the highly efficient charge-to-spin conversion.

3 | Conclusion

In summary, we have experimentally realized a robust FPM state within atomically engineered SRO/CTO SLs, where an unconventional out-of-plane B-site polar distortion resides directly within the itinerant ferromagnetic RuO_6 network. Thanks to the robust and intrinsic entanglement between polarization, ferromagnetism, and metallic conduction within the same lattice site, the resulting FPM shows magnetization self-switching at an ultra-low threshold of 2.5×10^5 A cm^{-2}, which is the lowest among all reported oxide systems and is approximately two orders of magnitude lower than that of conventional heavy-metal/ferromagnet heterostructures. Additionally, the device achieves a switching ratio of 75%, the highest value reported among self-switching systems to date. Our findings not only establish a general strategy for extracting polarity from non-polar perovskites but also position FPMs as a premier platform for energy-efficient, single-layer spintronic technologies.

4 | Methods

4.1 | Sample Fabrication and Characterizations

High-quality $[SRO/CTO]_{10}$ SL were epitaxially grown on (001)-oriented STO substrate by the technique of pulsed laser deposition (KrF, $\lambda = 248$ nm). During film growth, the substrate temperature was kept at 650°C, and the oxygen pressure was set to 20 Pa. The adopted fluence of the laser pulse was 1.2 J/cm^2, and the repetition rate was 2 Hz. The deposition rate for the SRO and CTO layers has been carefully calibrated by the technique of small-angle X-ray reflectivity (XRR, see Figure S1). The surface morphology of as-prepared films was measured by atomic force microscopy (AFM, SPI 3800N, Seiko). The crystal structure was determined by a high-resolution X-ray diffractometer (D8 Discover, Bruker) with Cu-Kα radiation. The magnetic properties were measured by a Quantum Design vibrating sample magnetometer (VSM-SQUID) in the temperature range of 5–300 K, with the maximal magnetic field of 7 T. The magnetic field was applied along the out-of-plane direction or the in-plane direction of the (001) films.

4.2 | Scanning Transmission Electron Microscopy

Multislice electron ptychography (MEP), a newly developed scanning transmission electron microscopy (STEM) technique that solves the inverse problem of electron scattering to obtain high-resolution and high-precision measurements of atomic structure, including both light and heavy atoms. Four-dimensional STEM (4D-STEM) electron diffraction datasets were acquired using a probe-aberration corrected JEOL NEOARM 200F equipped with a DECTRIS ARINA fast-readout detector at 200 kV. MEP reconstructions were performed using foldslice with similar parameters in previous publications (Z. Chen, et al., Science 372, 826 (2021)). Electron-transparent samples were prepared by Ga+ focused ion beam (FIB, FEI Strata 400) with progressively decreased beam energy from 30 to 2 keV to reduce ion-damage. EELS measurement was performed with a dispersion of 0,5 eV/pixel on a double aberration corrected Thermofisher Scientific Titan 80–300 microscope at the University of Antwerp, Belgium, operated at 300 kV, with a convergence semi-angle of 21mrad, collection angle of 64mrad and acquisition time of 0,2s/pixel in dual EELS mode. Raw data is presented after background subtraction.

4.3 | In-Plane Polarization Measurement (Normal Incidence)

0°-SHG measurements were performed using a Ti: sapphire femtosecond laser system ($\hbar\omega = 1.55$ eV, pulse width $\approx$ 100 fs, repetition rate 80 MHz) as the fundamental light source. The beam was focused onto the sample surface with a 50× microscopy objective, producing a spot size of approximately 1 μm. The average power of the incident beam was kept at 8 mW to avoid laser-induced heating or damage. All measurements were conducted at a fixed incident angle of 0° (defined between the sample normal and incident beam direction), with a temperature of 300 K. The polarization state of the fundamental beam was controlled using a half-wave plate and linear polarizer. Two distinct polarization configurations were systematically investigated. Specifically, the polarization of the incident light is parallel to the detection polarization direction of the output light (XX configuration), and the polarization of the incident light is perpendicular to the detection polarization direction of the output light (XY configuration). For each channel, the polarization-dependent SHG patterns were obtained by rotating 360°.

4.4 | Out-of-Plane Polarization Measurement (Oblique-Incidence)

45°-SHG measurements were performed using a Ti: sapphire femtosecond laser system ($\hbar\omega = 1.55$ eV, pulse width $\approx$ 150 fs, repetition rate 1 kHz) as the fundamental light source. The laser

pulses were focused onto the sample surface using a plano-convex lens ($f = 200$ mm), producing a spot size of approximately 200 μm, with the incident beam power maintained at 1 mW (average power) to prevent sample damage. All measurements were conducted at a fixed incident angle of 45° (defined between the sample normal and incident beam direction), with temperature-dependent studies spanning 77 to 300 K. The polarization state of the fundamental beam was controlled using a half-wave plate and linear polarizer. Four distinct polarization configurations were systematically investigated: Specifically, fundamental polarization fixed parallel or perpendicular (P_{in} or S_{in}) to the incidence plane while rotating the analyzer through 360°; Analyzer fixed parallel or perpendicular (P_{out} or S_{out}) to the incidence plane while rotating the fundamental polarizer through 360°.

4.5 | Device Fabrication and Electrical Measurement

The films were fabricated into Hall bar devices with a channel width and length of 10 and 40 μm, respectively, by ultraviolet photolithography and Ar ion milling. Afterward, Au was sputtered to produce four electrode terminals. The transport measurements were performed in a Quantum Design physical property measurement system (PPMS). The Anomalous Hall Effect (AHE) was measured using a 10 μA DC current. For the SOT switching measurements, a weak external magnetic field H_x along the x direction to ensure deterministic magnetization switching. Under the continuous application of H_x, a short-pulsed writing current J_{pulse}, with a pulse width of 1 ms, was applied along the x direction of the Hall bar by a Keithley 6221 current source. To minimize Joule heating, a small pulsed reading current of 10 μA with a pulse width of 0.1 s was applied after a 0.2 s interval with no current flow. By measuring the ρ_H under the reading current, the magnetization state of the SL was determined.

4.6 | First-Principles Calculations

DFT calculations were performed using the Vienna Ab initio Simulation Package (VASP) [59] with the Perdew-Burke-Ernzerh of exchange-correlation functional [60]. The electron-ion interactions were described using the projected augmented wave (PAW) method [61, 62] with a cutoff energy of 500 eV. The Brillouin zone was sampled using a Monkhorst-Pack k-mesh of 5×5×1. The experimental lattice constant was used while the atomic positions were fully relaxed until the residual force converged to 10^{-2} eV/Å. The spin-orbit coupling was included during electronic structure calculations, and the spin-projected band structure was drawn by the VASPKIT software package [63, 64].

Author Contributions

Y.Z.C. and Y.S.C. designed the concept and experiments. W.X.S. carried out the samples fabrication and performed the half-order diffraction peak, magnetic, electrical transport and SOT switching measurements. H.L. and Z.Q.D. carried out high-resolution STEM and ptychography experiments and reconstructions under the supervision of Z.C. N.G. performed EELS measurements. D.H. and Z.W. carried out the SHG measurements under the supervision of G.Z.S. H.J.W. formulated the theoretical models, carried out the first-principles calculations under the supervision of Y.C.L. Y.X. did the group theoretical analysis under the supervision of J.T.Z. J.H.C. contributed to the device fabrication. D.M.T. and H.Z. contributed to the SOT switching measurements. T.L.Z. and J.J.L. contributed to the magnetic measurements. Z.Y. contributed to the calculations of Rashba-split electronic band structures. B.W.Y., J.Z., J.W., Z.Z.Z., B.G.L., J.V., F.X.H., J.R.S. and B.G.S. discussed on physical mechanisms and data interpretation. All authors discussed the results, interpretations, and wrote the manuscript.

Acknowledgements

The authors thank the support from the National Key Research and Development Program of China (2023YFA1406400), the Science Center of the National Science Foundation of China (52088101), the National Key Research and Development Program of China (2021YFA1400300, 2023YFA1607400, 2023YFA1406003, 2022YFA1403302), the National Natural Science Foundation of China (12504157, 51327806, T2394472, T2394470, 12274443, 12595332, 1242240, 12422407, 52273227 and U22A6005), the Postdoctoral Fellowship Program and China Postdoctoral Science Foundation under Grant Number GZC20252236 and 2025M783454, the European Union's Horizon 2020 research and innovation program under Grant Agreement No. 823717-ESTEEM3, the Strategic Priority Research Program (B) of the Chinese Academy of Sciences (Grant Number. XDB1720000). We also thank the SM1 of the Steady High Magnetic field facility, CAS (https://cstr.cn/31125.02.SHMFF.SM1.MO) for the assistance on the experiment. This work was also supported by Shanghai Synchrotron Radiation Facility (BL02U2, BL07U and BL08U1A) and the Synergetic Extreme Condition User Facility (SECUF). We thank Prof. Zhe Yuan for fruitful discussions.

Conflicts of Interest

The authors declare no conflicts of interest.

Data Availability Statement

The authors declare that data generated in this study are provided in the paper and the Supporting Information file. Further datasets are available from the corresponding author upon request.

References

1. J. Jackson, *Classical Electrodynamics*, 3rd edn (John Wiley & Sons, 1999).

2. M. Lezaic, "Clockwork at the Atomic Scale," *Nature* 533 (2016): 38–39, https://doi.org/10.1038/nature17890.

3. P. W. Anderson and E. I. Blount, "Symmetry Considerations on Martensitic Transformations: "Ferroelectric" Metals?," *Physical Review Letters* 14 (1965): 217–219, https://doi.org/10.1103/PhysRevLett.14.217.

4. Y. Shi, Y. Guo, X. Wang, et al., "A Ferroelectric-Like Structural Transition in a Metal," *Nature Materials* 12 (2013): 1024–1027, https://doi.org/10.1038/nmat3754.

5. T. H. Kim, D. Puggioni, Y. Yuan, et al., "Polar Metals by Geometric Design," *Nature* 533 (2016): 68–72, https://doi.org/10.1038/nature17628.

6. T. Kolodiazhnyi, M. Tachibana, H. Kawaji, J. Hwang, and E. Takayama-Muromachi, "Persistence of Ferroelectricity in $BaTiO_3$ Through the Insulator-Metal Transition," *Physical Review Letters* 104 (2010): 147602, https://doi.org/10.1103/PhysRevLett.104.147602.

7. T. Zhu, X.-Z. Lu, T. Aoyama, et al., "Thermal Multiferroics in All-Inorganic Quasi-Two-Dimensional Halide Perovskites," *Nature Materials* 23 (2024): 182–188, https://doi.org/10.1038/s41563-023-01759-y.

8. T. Zhu, F. Orlandi, P. Manuel, et al., "Directed Synthesis of a Hybrid Improper Magnetoelectric Multiferroic Material," *Nature Communications* 12 (2021): 4945, https://doi.org/10.1038/s41467-021-25098-1.

9. N. A. Benedek and C. J. Fennie, "Hybrid Improper Ferroelectricity: A Mechanism for Controllable Polarization-Magnetization Coupling," *Physical Review Letters* 106 (2011): 107204, https://doi.org/10.1103/PhysRevLett.106.107204.

10. J. M. Rondinelli and C. J. Fennie, "Octahedral Rotation-Induced Ferroelectricity in Cation Ordered Perovskites," *Advanced Materials* 24 (2012): 1961–1968, https://doi.org/10.1002/adma.201104674.

11. Y. Zhang, J. Wang, and P. Ghosez, "Unraveling the Suppression of Oxygen Octahedra Rotations in $A_3B_2O_7$ Ruddlesden-Popper Compounds: Engineering Multiferroicity and Beyond," *Physical Review Letters* 125 (2020): 157601, https://doi.org/10.1103/PhysRevLett.125.157601.

12. X.-Z. Lu, H.-M. Zhang, Y. Zhou, et al., "Out-of-Plane Ferroelectricity and Robust Magnetoelectricity in Quasi-Two-Dimensional Materials," *Science Advances* 9 (2023): adi0138, https://doi.org/10.1126/sciadv.adi0138.

13. H. L. B. Boström, M. S. Senn, and A. L. Goodwin, "Recipes for Improper Ferroelectricity in Molecular Perovskites," *Nature Communications* 9 (2018): 2380.

14. J. Zhang, X. Shen, Y. Wang, et al., "Design of Two-Dimensional Multiferroics With Direct Polarization-Magnetization Coupling," *Physical Review Letters* 125 (2020): 017601, https://doi.org/10.1103/PhysRevLett.125.017601.

15. S. Lei, M. Gu, D. Puggioni, et al., "Observation of Quasi-Two-Dimensional Polar Domains and Ferroelastic Switching in a Metal, $Ca_3Ru_2O_7$," *Nano Letters* 18 (2018): 3088–3095, https://doi.org/10.1021/acs.nanolett.8b00633.

16. I. Markovic, M. D. Watson, O. J. Clark, et al., "Electronically Driven Spin-Reorientation Transition of the Correlated Polar Metal $Ca_3Ru_2O_7$," *Proceedings of the National Academy of Sciences* 117 (2020): 15524–15529, https://doi.org/10.1073/pnas.2003671117.

17. Y. Zhou, X. Shu, Y. Zhang, et al., "Geometry-Driven Polar Antiferromagnetic Metallicity in a Double-Layered Perovskite Cobaltate," *Nature Materials* 25 (2026): 231–237, https://doi.org/10.1038/s41563-025-02392-7.

18. J. Zhang, S. Shen, D. Puggioni, et al., "A Correlated Ferromagnetic Polar Metal by Design," *Nature Materials* 23 (2024): 912–919, https://doi.org/10.1038/s41563-024-01856-6.

19. Y. Jiang, J. Niu, C. Wang, et al., "Experimental Demonstration of Tunable Hybrid Improper Ferroelectricity in Double-Perovskite Superlattice Films," *Nature Communications* 15 (2024): 5549, https://doi.org/10.1038/s41467-024-49707-x.

20. Y. Jiang, D. Xue, J. Niu, et al., "Tuning Perpendicular Magnetic Anisotropy Compatible With Hybrid Improper Ferroelectricity via a Geometrical Route," *Physical Review Letters* 135 (2025): 046801, https://doi.org/10.1103/q237-k8yg.

21. K. Zhang, S. Han, Y. Lee, et al., "Gigantic Current Control of Coercive Field and Magnetic Memory Based on Nm-Thin Ferromagnetic van Der Waals Fe_3GeTe_2," *Advanced Materials* 33 (2021): 2004110.

22. Ø. Johansen, V. Risinggård, A. Sudbø, J. Linder, and A. Brataas, "Current Control of Magnetism in Two-Dimensional Fe_3GeTe_2," *Physical Review Letters* 122 (2019): 217203, https://doi.org/10.1103/PhysRevLett.122.217203.

23. Y. Deng, M. Wang, Z. Xiang, et al., "Room-Temperature Highly Efficient Nonvolatile Magnetization Switching by Current in van der Waals Fe_3GaTe_2 Devices," *Nano Letters* 24 (2024): 9302–9310, https://doi.org/10.1021/acs.nanolett.4c02227.

24. K.-X. Zhang, H. Ju, H. Kim, et al., "Broken Inversion Symmetry in van der Waals Topological Ferromagnetic Metal Iron Germanium Telluride," *Advanced Materials* 36 (2024): 2312824, https://doi.org/10.1002/adma.202312824.

25. K.-X. Zhang, S. Cheon, H. Kim, et al., "Current-Driven Collective Control of Helical Spin Texture in van der Waals Antiferromagnet," *Physical Review Letters* 134 (2025): 176701, https://doi.org/10.1103/PhysRevLett.134.176701.

26. K.-X. Zhang, S. Lee, W. Cho, and J.-G. Park, "Current Switching of Topological Spin Chirality in the van Der Waals Antiferromagnet $Co_{1/3}TaS_2$," *Advanced Materials* 38 (2026): 22943, https://doi.org/10.1002/adma.202522943.

27. G. Koster, L. Klein, W. Siemons, et al., "Structure, Physical Properties, and Applications of $SrRuO_3$ Thin Films," *Reviews of Modern Physics* 84 (2012): 253–298, https://doi.org/10.1103/RevModPhys.84.253.

28. H. Boschker, T. Harada, T. Asaba, et al., "Ferromagnetism and Conductivity in Atomically Thin $SrRuO_3$," *Physical Review X* 9 (2019): 011027.

29. J. R. Kim, J. Jang, K.-J. Go, et al., "Stabilizing Hidden Room-Temperature Ferroelectricity via a Metastable Atomic Distortion Pattern," *Nature Communications* 11 (2020): 4944, https://doi.org/10.1038/s41467-020-18741-w.

30. E. R. Hoglund, D.-L. Bao, A. O'Hara, et al., "Emergent Interface Vibrational Structure of Oxide Superlattices," *Nature* 601 (2022): 556–561, https://doi.org/10.1038/s41586-021-04238-z.

31. V. M. Edelstein, "Spin Polarization of Conduction Electrons Induced by Electric Current in Two-Dimensional Asymmetric Electron Systems," *Solid State Communications* 73 (1990): 233–235, https://doi.org/10.1016/0038-1098(90)90963-C.

32. A. Chernyshov, M. Overby, X. Liu, J. K. Furdyna, Y. Lyanda-Geller, and L. P. Rokhinson, "Evidence for Reversible Control of Magnetization in a Ferromagnetic Material by Means of Spin–Orbit Magnetic Field," *Nature Physics* 5 (2009): 656–659, https://doi.org/10.1038/nphys1362.

33. C. Ciccarelli, L. Anderson, V. Tshitoyan, et al., "Room-Temperature Spin–Orbit Torque in NiMnSb," *Nature Physics* 12 (2016): 855–860, https://doi.org/10.1038/nphys3772.

34. D. MacNeill, G. M. Stiehl, M. H. D. Guimaraes, R. A. Buhrman, J. Park, and D. C. Ralph, "Control of Spin–Orbit Torques Through Crystal Symmetry in WTe_2/Ferromagnet Bilayers," *Nature Physics* 13 (2017): 300–305, https://doi.org/10.1038/nphys3933.

35. R. Yoshimi, K. Yasuda, A. Tsukazaki, et al., "Current-Driven Magnetization Switching in Ferromagnetic Bulk Rashba Semiconductor (Ge, Mn)Te," *Science Advances* 4 (2018): aat9989.

36. A. Fert, R. Ramesh, V. Garcia, F. Casanova, and M. Bibes, "Electrical Control of Magnetism by Electric Field and Current-Induced Torques," *Reviews of Modern Physics* 96 (2024): 015005, https://doi.org/10.1103/RevModPhys.96.015005.

37. L. Liu, G. Zhou, X. Shu, et al., "Room-Temperature Spin-Orbit Torque Switching in a Manganite-Based Heterostructure," *Physical Review B* 105 (2022): 144419, https://doi.org/10.1103/PhysRevB.105.144419.

38. L. Liu, Q. Qin, W. Lin, et al., "Current-Induced Magnetization Switching in All-Oxide Heterostructures," *Nature Nanotechnology* 14 (2019): 939–944, https://doi.org/10.1038/s41565-019-0534-7.

39. Y. Jo, Y. Kim, S. Kim, et al., "Field-Free Spin–Orbit Torque Magnetization Switching in a Single-Phase Ferromagnetic and Spin Hall Oxide," *Nano Letters* 24 (2024): 7100–7107, https://doi.org/10.1021/acs.nanolett.4c01788.

40. H. Horiuchi, Y. Araki, Y. K. Wakabayashi, et al., "Single-Layer Spin-Orbit-Torque Magnetization Switching due to Spin Berry Curvature Generated by Minute Spontaneous Atomic Displacement in a Weyl Oxide," *Advanced Materials* 37 (2025): 2416091, https://doi.org/10.1002/adma.202416091.

41. I. M. Miron, K. Garello, G. Gaudin, et al., "Perpendicular Switching of a Single Ferromagnetic Layer Induced by in-Plane Current Injection," *Nature* 476 (2011): 189–193, https://doi.org/10.1038/nature10309.

42. L. Liu, C.-F. Pai, Y. Li, H. W. Tseng, D. C. Ralph, and R. A. Buhrman, "Spin-Torque Switching With the Giant Spin Hall Effect of Tantalum," *Science* 336 (2012): 555–558, https://doi.org/10.1126/science.1218197.

43. L. Liu, O. J. Lee, T. J. Gudmundsen, D. C. Ralph, and R. A. Buhrman, "Current-Induced Switching of Perpendicularly Magnetized Magnetic Layers Using Spin Torque From the Spin Hall Effect," *Physical*

Review Letters 109 (2012): 096602, https://doi.org/10.1103/PhysRevLett.109.096602.

44. S. J. May, J.-W. Kim, J. M. Rondinelli, et al., "Quantifying Octahedral Rotations in Strained Perovskite Oxide Films," *Physical Review B* 82 (2010): 014110, https://doi.org/10.1103/PhysRevB.82.014110.

45. I. C. Tung, P. V. Balachandran, J. Liu, et al., "Connecting Bulk Symmetry and Orbital Polarization in Strained $RNiO_3$ Ultrathin Films," *Physical Review B* 88 (2013): 205112, https://doi.org/10.1103/PhysRevB.88.205112.

46. A. M. Glazer, "The Classification of Tilted Octahedra in Perovskites," *Acta Crystallographica Section B Structural Crystallography and Crystal Chemistry* 28 (1972): 3384–3392, https://doi.org/10.1107/S0567740872007976.

47. A. Glazer, "Simple Ways of Determining Perovskite Structures," *Foundations of Crystallography* 31 (1975): 756–762.

48. Z. Chen, Y. Jiang, Y.-T. Shao, et al., "Electron Ptychography Achieves Atomic-Resolution Limits Set by Lattice Vibrations," *Science* 372 (2021): 826–831, https://doi.org/10.1126/science.abg2533.

49. D. Kan, R. Aso, R. Sato, M. Haruta, H. Kurata, and Y. Shimakawa, "Tuning Magnetic Anisotropy by Interfacially Engineering the Oxygen Coordination Environment in a Transition Metal Oxide," *Nature Materials* 15 (2016): 432–437, https://doi.org/10.1038/nmat4580.

50. Y. Yuan, Y. Lu, G. Stone, et al., "Three-Dimensional Atomic Scale Electron Density Reconstruction of Octahedral Tilt Epitaxy in Functional Perovskites," *Nature Communications* 9 (2018): 5220, https://doi.org/10.1038/s41467-018-07665-1.

51. E. Bousquet, M. Dawber, N. Stucki, et al., "Improper Ferroelectricity in Perovskite Oxide Artificial Superlattices," *Nature* 452 (2008): 732–736, https://doi.org/10.1038/nature06817.

52. S. Shen, Z. Li, Z. Tian, W. Luo, S. Okamoto, and P. Yu, "Emergent Ferromagnetism With Fermi-Liquid Behavior in Proton Intercalated $CaRuO_3$," *Physical Review X* 11 (2021): 021018.

53. D. Hou, J. Bi, J. Yang, et al., "Polar Metals With Coexisting Ferroelectricity and High-Density Conduction Electrons," *Applied Physics Letters* 124 (2024): 062903, https://doi.org/10.1063/5.0187330.

54. J. Varignon, L. Vila, A. Barthélémy, and M. Bibes, "A New Spin for Oxide Interfaces," *Nature Physics* 14 (2018): 322–325, https://doi.org/10.1038/s41567-018-0112-1.

55. H. Xu, H. Li, N. Gauquelin, et al., "Giant Tunability of Rashba Splitting at Cation-Exchanged Polar Oxide Interfaces by Selective Orbital Hybridization," *Advanced Materials* 36 (2024): 2313297, https://doi.org/10.1002/adma.202313297.

56. H. Zhang, X. Chen, T. Wang, et al., "Room-Temperature, Current-Induced Magnetization Self-Switching in a Van Der Waals Ferromagnet," *Advanced Materials* 36 (2024): 2308555, https://doi.org/10.1002/adma.202308555.

57. Y. Tao, C. Sun, W. Li, et al., "Field-Free Spin–Orbit Torque Switching in L 1-FePt Single Layer With Tilted Anisotropy," *Applied Physics Letters* 120 (2022): 102405, https://doi.org/10.1063/5.0077465.

58. M. Jiang, H. Asahara, S. Sato, et al., "Efficient Full Spin–Orbit Torque Switching in a Single Layer of a Perpendicularly Magnetized Single-Crystalline Ferromagnet," *Nature Communications* 10 (2019): 2590, https://doi.org/10.1038/s41467-019-10553-x.

59. G. Kresse and J. Furthmüller, "Efficient Iterative Schemes for Ab Initio Total-energy Calculations Using a Plane-wave Basis Set," *Physical Review B* 54 (1996): 11169–11186, https://doi.org/10.1103/PhysRevB.54.11169.

60. J. P. Perdew, K. Burke, and M. Ernzerhof, "Generalized Gradient Approximation Made Simple," *Physical Review Letters* 77 (1996): 3865–3868, https://doi.org/10.1103/PhysRevLett.77.3865.

61. P. E. Blöchl, "Projector Augmented-Wave Method," *Physical Review B* 50 (1994): 17953–17979.

62. G. Kresse and D. Joubert, "From Ultrasoft Pseudopotentials to the Projector Augmented-Wave Method," *Physical Review B* 59 (1999): 1758–1775, https://doi.org/10.1103/PhysRevB.59.1758.

63. V. Wang, N. Xu, J.-C. Liu, G. Tang, and W.-T. Geng, "VASPKIT: A User-Friendly Interface Facilitating High-Throughput Computing and Analysis Using VASP Code," *Computer Physics Communications* 267 (2021): 108033, https://doi.org/10.1016/j.cpc.2021.108033.

64. J. Cheng, B. F. Miao, Z. Liu, et al., "Coherent Picture on the Pure Spin Transport Between Ag/Bi and Ferromagnets," *Physical Review Letters* 129 (2022): 097203, https://doi.org/10.1103/PhysRevLett.129.097203.

Supporting Information

Additional supporting information can be found online in the Supporting Information section.

Supporting File: adma74269-sup-0001-SuppMat.docx.